ADVANCED INTELLIGENT SYSTEMS
Open Access
www.advintellsyst.com

Flexure Variable Stiffness Actuators

*Frederic H. Giraud, Mustafa Mete, and Jamie Paik**

Series elastic actuators (SEAs) and variable elastic actuators (VSAs) provide shock resistance, energy storage, and stable force control. However, they usually require extra springs, mechanical parts, and transmissions, increasing size, weight, number of moving parts, and reducing the mechanical efficiency. In particular, this mechanical complexity is one of the significant challenges in the design of wearable and scalable force feedback devices. In this article, flexure variable stiffness actuators (F-VSAs), which combine kinematic transmission, elasticity, and stiffness modulation via a network of folding patterns using flexure hinges, are presented. Thus, F-VSAs allow the creation of robots benefiting from the advantages of SEAs and VSAs without hindering form factor or mechanical efficiency. To illustrate the design strategy of F-VSAs, a 4-design-of-freedom (DoF) robot that provides stiffness and force output is presented. An analytical model that estimates the inherent stiffness and the end-effector force output for any given configuration of the folding pattern is proposed. Finally, stiffness modulation and force control of the robot are implemented and good agreement with the predictions from the model is observed. Thus, this novel design strategy allows the creation of compact and scalable robots with stiffness and force output for wearable, rehabilitation, and haptic applications.

1. Introduction

Achieving safe human–robot interaction becomes crucial with the developments of many robotics fields such as rehabilitation, assistance, service, wearables, and haptics. To this end, researchers have explored alternatives to conventional fully rigid actuation methods such as soft actuators and electromechanical motors combined with elastic elements. Soft actuators using pneumatics,[1] hydraulics,[2,3] elastomers,[4] and smart materials[5] have proven to enhance the user's safety.[6,7] This category also includes variable stiffness soft actuators relying on jamming[8,9] or smart materials.[5,10] However, soft actuators suffer from complex modeling, difficult control, low actuation speed, and bulky power supplies.[11,12] This study focuses on the alternative compliant actuation method that uses conventional actuators coupled with elastic elements such as series elastic actuators (SEAs) and variable stiffness actuators (VSAs), which show better performance regarding the aforementioned soft actuators limitations.

SEAs[13–19] consist of actuators connected to elastic elements and loads in series.[20] The elastic elements serve three main purposes: 1) storing and releasing energy, thus improving energy efficiency,[21] 2) converting the force control problem to a position control problem due to the well-defined relationship between elastic deformation and output force,[20] and 3) reducing peak forces on the motor and user during impact, thereby improving safety.[22] However, SEAs usually hinder the actuator's bandwidth, thus limiting the performance. Moreover, they cannot adapt their stiffness with respect to the different loads and conditions, which can cause undesired oscillations.[23]

Unlike SEAs, VSAs[24–26] tune the stiffness of their elastic elements to adapt their compliance and bandwidth to changing environments and conditions. For example, higher-stiffness configurations enable faster response and better fidelity performance, while lower-stiffness configurations reduce the impact of collision and achieve safer and more stable force and torque output. VSAs are categorized into three general groups based on how they vary their stiffness: spring pretension, changing transmission, and changing physical properties of springs.[20,27] While each of these categories has specific assets and liabilities, they suffer from a common limitation: the need for extra components and mechanisms[20,28,29] which leads to an increase in complexity, weight, size, and time of assembly.[30] These challenges set back the ability of VSAs to target applications requiring miniaturized devices with multi-degree-of-freedom (DoF) force outputs[16] such as wearable devices and haptics.

To address mechanical complexity issues of VSAs, researchers have investigated the use of flexure hinges for compliant mechanisms. Flexure-based mechanisms enable the design of miniaturized, compact, and lightweight multi-DoF mechanisms and robots with a reduced number of components.[31–36] In VSA, existing studies[27,37–39] use flexure hinges and mechanisms as variable stiffness elements. In these works, the flexure mechanisms only serve as compliant springs and attachments connecting the motor to the linkages or other transmission components, which do not solve the complexity issues of VSAs. Moreover, flexure-based mechanisms' stiffness is often found by

F. H. Giraud, M. Mete, J. Paik
Reconfigurable Robotics Laboratory
École Polytechnique Fédérale de Lausanne (EPFL)
1015 Lausanne, Switzerland
E-mail: jamie.paik@epfl.ch

The ORCID identification number(s) for the author(s) of this article can be found under https://doi.org/10.1002/aisy.202100282.

DOI: 10.1002/aisy.202100282

experimental characterizations due to difficult modeling. This is accentuated in mechanisms with complex folding patterns and closed kinematics chains.

In this article, we present flexure variable stiffness actuators (F-VSAs) that address the mechanical complexity of VSAs by combining kinematic transmission, elasticity, and variable stiffness in repeating folding patterns, as shown in **Figure 1**. The folding patterns are composed of flexure hinges, which act as virtual springs and add elasticity to the system. By virtue of their design, the overall stiffness of F-VSAs is a function of the folding pattern configuration, which can be modulated using actuators. The flexure-based folds serve as links and joints defining the kinematics of a system. Thus, by combining all in one, they do not need extra elastic elements and mechanisms to achieve variable stiffness. Furthermore, our general stiffness modeling approach based on the matrix structural analysis (MSA) method enables the estimation of the stiffness of F-VSAs at different configurations for any folding pattern. Hence, the model allows the modulation of stiffness and force output by the active control of the folding pattern configuration.

Using this method, we create a 4-DoF F-VSA system that provides stiffness and force output. The device uses eight motors at its periphery to actuate the central end-effector and control stiffness and force output. We conduct stiffness modulation and force control experiments and verify that we can modulate the stiffness and force output of the system. The proposed model successfully predicts the actual behavior in the entire workspace. Thus, our F-VSA method proposes a new paradigm toward compact multi-DoF robot designs for many robotics fields such as wearables, rehabilitation, and haptics, which require mechanical force and torque control stability.

The main contributions of this work are: 1) F-VSAs, A novel actuation system design that improves mechanical complexity and compactness of state-of-the-art VSAs; 2) a comprehensive modeling of F-VSAs to map achievable stiffness for any configuration; and 3) design, prototyping, and control of a 4-DoF F-VSA system and experimental validation of the prototype.

2. Flexure Variable Stiffness Actuator Overview

This section describes the F-VSA and compares design and capabilities with other elastic actuators such as SEAs and VSAs. To allow force and stiffness control of our system, we also introduce a method to model the stiffness that can be applied to any F-VSA design.

2.1. F-VSA Design and Features

F-VSA is an alternative to SEAs and VSAs. It reduces the mechanical complexity to enable miniaturized robot design providing force and stiffness output with a compact form factor. To illustrate how the F-VSA differs from SEAs and VSAs, we represent these three concepts in **Figure 2**. The SEAs and VSAs are composed of the following elements.

End-Effector: The point of the system that interacts with the environment is end-effector. Elastic actuators aim at controlling the force and position at the end-effector.

Elastic Elements: They add compliance to the system and generate force and torque based on their compression or tension. For SEAs and VSAs, springs are often used as elastic elements.

Actuators: They control the elastic elements and therefore the force output at the end-effector.

Transmissions: They define the kinematics, speed, and force characteristics of the actuator.

Unlike SEAs, VSAs add extra actuators, elastic elements, connectors, friction reducers, and mechanisms with different approaches to achieve variable stiffness,[20,30] increasing the mechanical complexity. As an alternative to SEAs and VSAs, F-VSAs utilize flexure patterns as both kinematic transmission and elastic elements. The inherent stiffness of the flexure joints used in the transmission defines the overall stiffness of the system. Therefore, by changing the configuration, one can vary the overall stiffness and control the force output and position of the end-effector. Furthermore, the flexure joint reduces the number of mechanical parts and components required for achieving multi-DoF structures, as shown in Figure 2b. Thus, this method significantly reduces the mechanical complexity and bulkiness of

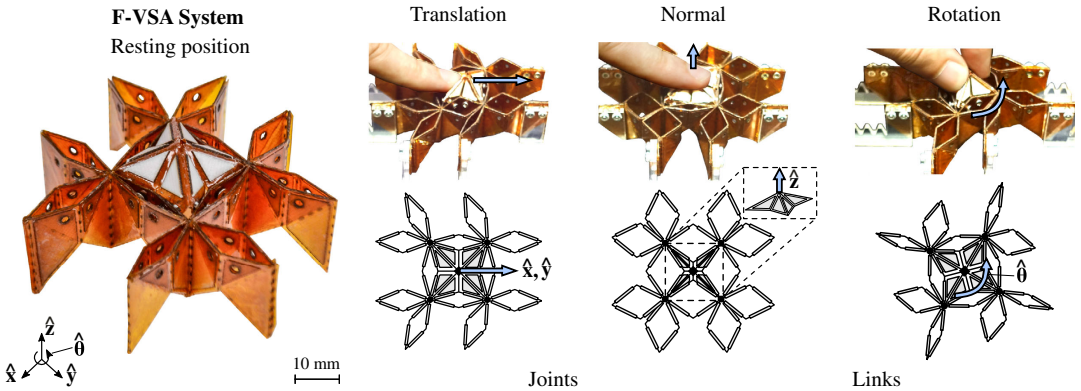

Figure 1. The F-VSA system is composed of several compliant four-bar linkages connected to each other with folding hinges and the out-of-plane mechanism in the center serving as end-effector. These diamonds dictate the kinematics of the platform and serve as series elastic elements, thanks to their built-in compliance, which act as virtual springs. Moreover, by reconfiguring the diamonds' geometry, this platform can vary the stiffness of these virtual springs. Thus, this device can render variable stiffness and forces by controlling its configuration. It allows the design of compact devices, thanks to the compliant diamond patterns and hinges that combine transmission mechanisms, elastic elements, and variable stiffness.

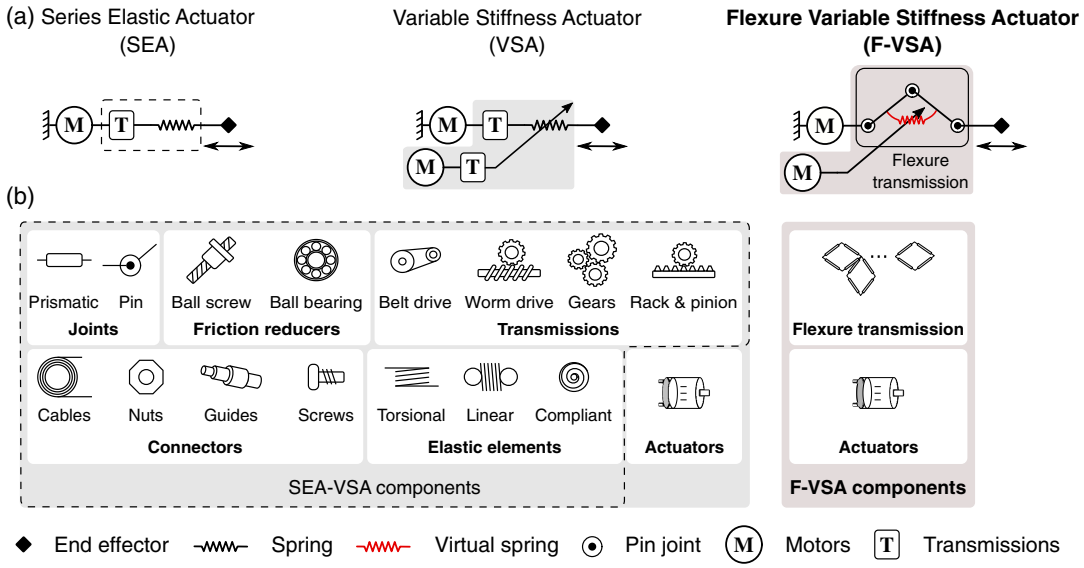

Figure 2. Comparison of SEAs, VSAs, and F-VSAs. SEAs are generally composed of many types of components such as joints, transmissions, connectors, elastic elements, and friction reducers. SEAs cannot adapt the stiffness of their springs to changing conditions. On the other hand, VSAs can vary the stiffness of their elastic elements using additional aforementioned components and extra actuators. However, they suffer from mechanical complexity and bulkiness. As a new approach, F-VSAs incorporate all these components in their flexure transmission, which has virtual springs at its joints and defines the system's kinematics. We can control the configuration of the flexure transmission to dictate the overall stiffness of the system. Thus, F-VSA method offers a solution to the mechanical complexity issue of VSAs. These three approaches and their design components are summarized in (a) and (b).

the system by combining many functionalities in flexure transmission and ensuring mechanical efficiency and reduced assembly complexity.

Although improving the compactness of a force–output system by reducing the mechanical complexity, F-VSAs come with a stiffness modeling challenge, especially for multi-DoF systems. They require a general stiffness modeling of flexure transmission to estimate the overall stiffness at any configuration. The model needs to take into account material properties, geometric parameters, and any type of kinematic chains. For these reasons, we use the MSA method for stiffness modeling of F-VSAs.

2.2. MSA Method Overview

To actively control the stiffness and force output of F-VSAs by changing their configuration, we study its all-inclusive stiffness model by considering initial and boundary conditions, material properties, and dimensions. In this article, we use the MSA method[40] to model the stiffness of F-VSAs. Compared with two other stiffness modeling methods virtual joint modeling (VJM)[41] and finite-element analyses (FEA)[42] in the literature, the MSA has less computational expensiveness than the FEA method and also considers the flexibility of the links compared with VJM. Particularly, Klimchik et al.[43] presents a systematic approach to applying MSA method to a large range of mechanisms in their study. Their approach is compatible with overconstrained parallel mechanisms with closed-loop chains, flexible links, and joints, making it the most suitable method to model the stiffness of F-VSAs.

The MSA method proposed by Klimchik et al.[43] can be achieved in four steps summarized in Figure 6a.

2.2.1. System Description

System description describes the mechanical system as a collection of elements which is composed of nodes, links, joints, platform, and boundary conditions.

1) The nodes are the basic elements of the system. The force–-displacement relations between them are what define links and joints. A link is described with two nodes, while a joint can connect more than two nodes together. In addition, boundary conditions affect some nodes that can be under external loading. This is the case for the end-effector node.

2) Joints can be rigid, passive, or elastic and connect link, base, and platform. While rigid joints fully transmit displacement and force conditions between nodes, passive and elastic joints are defined with one or multiple DoF in rotation and translation. Finally, the force transmitted along the free axis can be null for the passive joints or defined by a stiffness matrix for the elastic joint.

3) Links can be either rigid or flexible. While rigid links assume that the distance between nodes is kept constant, flexible links are defined using the stiffness matrix of the element. The latter can have a beam shape to simplify the problem or a complex geometry from which stiffness coefficients are extracted using a computer-aided design (CAD)-based method.[44]

4) In a parallel manipulator, the platform connects the different branches of the system to the end-effector node. Similar to the links, the platform can be either rigid or flexible by including stiffness coefficients.

5) The boundary conditions are defined by the connections between the aforementioned elements and the system base. This category also includes the external wrenches applied on some of the nodes, necessary to constrain the system entirely.

2.2.2. Force–Displacement Relations

For each element, we write all force–displacement relations in the matrix form as follows.

$$[\mathbf{A_W} \quad \mathbf{A_{\Delta t}}] \cdot \begin{bmatrix} \mathbf{W} \\ \mathbf{\Delta t} \end{bmatrix} = [\mathbf{b}_0] \tag{1}$$

$\mathbf{W}$ and $\mathbf{\Delta t}$ correspond respectively to the wrench and displacements variables along the three rotation and translation axes. $\mathbf{A_W}$ and $\mathbf{A_{\Delta t}}$ are the coefficients matrices corresponding to $\mathbf{W}$ and $\mathbf{\Delta t}$, respectively. $\mathbf{b}_0$ is the right-hand side of the corresponding equation/constraints, such as preloadings or external wrenches.

If we write (1) for links and joints with two nodes, we have 12 equations corresponding to the number of rows. In the case of joints linking three or a higher number of nodes, we will have six more equations per node. Finally, we have six equations for the boundary conditions.

2.2.3. Matrix Aggregation

This method requires the concatenation of all the element matrices of Equation (1) into a larger linear matrix equation. The latter should contain the end-effector node equations in the last rows, such as

$$\begin{bmatrix} \mathbf{A} & \mathbf{B} \\ \mathbf{C} & \mathbf{D} \end{bmatrix} \cdot \begin{bmatrix} \boldsymbol{\mu} \\ \mathbf{\Delta t}_e \end{bmatrix} = \begin{bmatrix} \mathbf{b} \\ \mathbf{W}_e \end{bmatrix} \tag{2}$$

with $\mathbf{B}$, $\mathbf{C}$, and $\mathbf{D}$ as the coefficients associated with the end-effector node and equations, and $\mathbf{A}$ the remaining equation coefficient. Force and displacement variables are aggregated in μ while $\mathbf{\Delta t}_e$ is a vector of the six displacement variables of the end-effector. Finally, $\mathbf{b}$ and $\mathbf{W}_e$ are the initial conditions of the different elements and end-effectors, respectively.

2.2.4. Solving the System

Consequently, we can derive the relation between end-effector displacement $\mathbf{\Delta t}_e$ and force $\mathbf{W}_e$ from the equation

$$\mathbf{W}_e = (\mathbf{D} - \mathbf{C} \cdot \mathbf{A}^{-1} \cdot \mathbf{B}) \cdot \mathbf{\Delta t}_e + \mathbf{C} \cdot \mathbf{A}^{-1} \cdot \mathbf{b} \tag{3}$$

from which one can extract the desired stiffness matrix

$$\mathbf{Kc} = \mathbf{D} - \mathbf{C} \cdot \mathbf{A}^{-1} \cdot \mathbf{B} \tag{4}$$

and the constant force component

$$\mathbf{W}_e^0 = \mathbf{C} \cdot \mathbf{A}^{-1} \cdot \mathbf{b} \tag{5}$$

To get a further understanding, we made an application example of the MSA method applied on a four-bar linkage in Appendix 7.3.

3. F-VSA System: A 4-DoF Device with Force and Stiffness Output

Based on the design method of Section 2.1, we created an F-VSA system as a proof of concept. Our compliant structure provides force transmission, series elasticity, and variable stiffness and force output. First, this section describes the design and working principle of the F-VSA system. Then, we demonstrate that we can manufacture the F-VSA elements using several methods. Finally, we described our structure to apply the analytic model of Section 2.2 and used it to develop a control strategy for the F-VSA system.

3.1. Design and Capabilities

We demonstrate the F-VSA design principle through a proof of concept shown in Figure 1. This design is a highly redundant kinematic structure used as a 4-DoF haptic system able to render force and stiffness output. It consists of a grid of 12 diamond patterns linked together by compliant pin joints and an out-of-plane mechanism in the center. The latter acts as the end-effector for user interaction and can move in translation in the $\hat{x}$, $\hat{y}$, and $\hat{z}$ axes, and rotation in the $\hat{z}$ axis. The external vertices of the outer eight diamond patterns are attached to linear servo motors through compliant hinge joints. The motors control the extension/contraction of the eight outer diamonds, as shown in **Figure 3**, which defines the input space of the device. These motors change the geometry of the outer diamond patterns, which changes the overall stiffness at the end-effector. When the diamonds are in the extended state, the stiffness is high, and when the diamonds are in the compressed state, the stiffness is low.

The F-VSA system is composed of the following types of repeating elements.

Diamond Pattern: This component primarily serves as the stiffness and transmission element of the device. It consists of four rigid tiles connected to each other with flexible hinges, such that it forms a closed-chain rhombus when viewed from the top. Its displacement is defined by the compression/extension in the diagonal directions.

Out-of-Plane Mechanism: The main objective of this component is to generate out-of-plane motion in the F-VSA. It is a transmission that consists of a square with compliant pin joints along the diagonals and the lines joining midpoints of opposite edges. This divides the square into eight triangles with joints that alternate their direction of rotation. When the corner points of the square are pushed in, the mechanism pushes the central point out of the plane, as shown in Figure 3a. Its displacement is thus defined by the planar motion of the corner points of the square and the out-of-plane motion of its central point. We design the compliant pin joints of the out-of-plane mechanism to have negligible compliance compared with the diamonds.

Actuator: This is the active component, whose main objective is to generate motion in the structure. It can be connected to either the diamond or the out-of-plane mechanism.

When combined together, networks of diamond and out-of-plane mechanisms can generate highly redundant motions with nonlinear stiffness characteristics. When different sections are

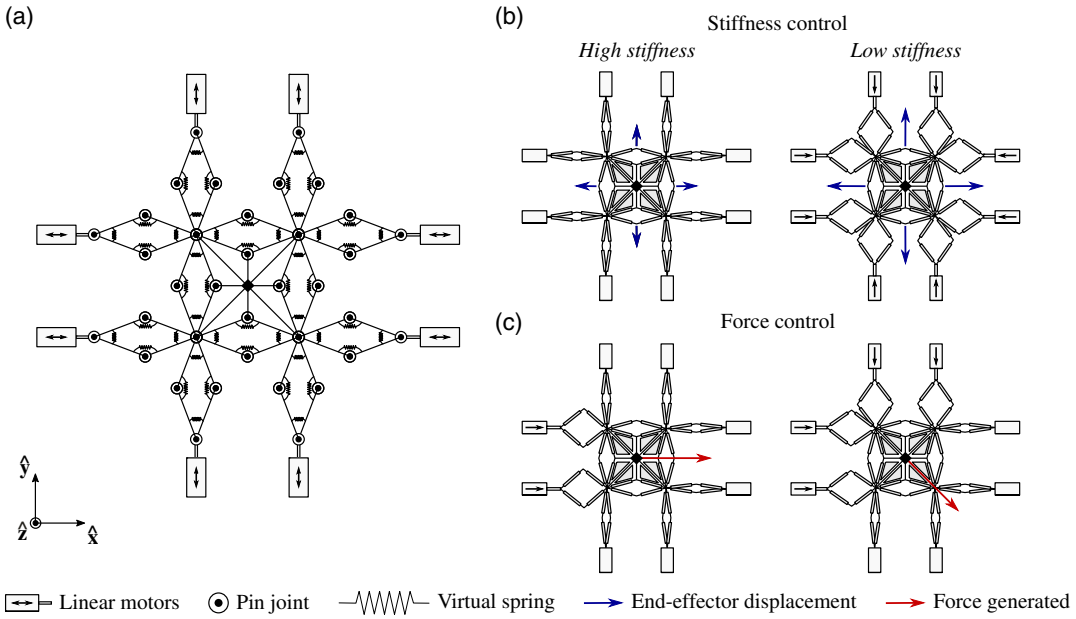

Figure 3. Working principle of the F-VSA system. a) The F-VSA system is composed of compliant joints that act as pin joints and virtual torsional springs. b) By controlling the configuration of the diamonds, we can vary and control the stiffness of the end-effector. c) Moreover, our device can generate force in a specific direction at the end-effector that can be controlled by changing the system's configuration.

actively controlled with actuating elements, we can get a controllable surface that is compact, compliant, capable of moving in multiple directions, and can generate a large range of force and stiffness output along multiple DoF. We consider two main types of outputs.

Stiffness Control: When deformed, internal restoring forces are developed at the joints of the device, which are transmitted to the end-effector when the latter moves. Due to the multiple joints in the system, this restoring force depends on the structure's geometry in addition to the materials used for making pin joints. By controlling the actuators, we can reconfigure the structure's geometry, thereby tuning the natural stiffness at the end-effector.

Force Control: The second way of producing force and stiffness output is by actively controlling the position of the motors. Due to the elasticity of the overall structure, these forces are generated indirectly through the deformation of the compliant joints.

3.2. Manufacturing Methods

Our platform relies on the stiffness of the compliant pin joint to modulate the force at the end-effector. Achieving such a device using conventional pin joints and springs is possible at the cost of a time-consuming assembly that would result in a bulkier platform. On the other hand, compliant joint combines spring and pin joint in a compact and assembly-free embodiment. They are also exempt from backlash, wear, and frictions and can be achieved through several manufacturing strategies. The choice of the latter depends on the application, the ability to tune the stiffness of the joints, and the fabrication time. We attempted to fabricate our device using the four following manufacturing processes.

Multimaterial 3D Printing: This technology benefits from all the advantages of conventional 3D printers and allows fast and assembly-free prototyping. We used Connex 500 to 3D print a diamond composed of flexible (Tango) and rigid (Vero) materials. With this technology, the stiffness of the joints is directly related to the material thickness and can be tuned by modifying the design parameters. However, we observed that the flexible material is prone to break after several folding of the joints.

Laser Sintering: This manufacturing process produces assembly-free and robust prototypes. We used the EOSINT P 395 to 3D print our complete device, using PA 2200 as material. This method uses a laser that sinters the PA 2200 powder layer by layer to create 3D structures. We designed a thin layer of the material to make compliant pin joints and tune their stiffness by modifying the layer's thicknesses. We create the links using a larger material thickness. However, laser resolution limits the material size, which does not allow the fabrication of low-stiffness joints.

Laser Cutting of Flexible Materials: This method uses a laser to cut a flexible material. We used a high-precision custom UV laser to cut a rubber layer of 1 mm thickness. This manufacturing method is fast, assembly free, and easily scalable. Similar to the laser-sintering process, joints and link stiffnesses are defined by the thickness, material, and design parameters of the layer. Nevertheless, larger stiffnesses require increased link and joint dimensions, which can be challenging for small devices.

Origami Manufacturing: This method consists of assembling layers of functional materials in 2D and folding the resulting stack to create a 3D structure. This manufacturing strategy allows the creation of compact, scalable, and highly customizable robots, known as Origami robots or Robogami.[31,33,34,45–49] We fabricated this prototype of the F-VSA system with Kapton for the flexural joints and fiberglass FR4 for rigid tiles. Kapton

has been proven to be a reliable and durable material that can withstand numerous folding cycles at high speed[50] and is therefore suitable for the F-VSA system's joints. Our origami-inspired layer-by-layer fabrication process is described in detail in Section 3.3. This manufacturing method allows tuning material property, design, and thickness to create durable joints and links with different properties. However, the downsides of this method are caused by the minimal assembly and folding process, which are time-consuming.

The resulting devices are shown in **Figure 4**. The aforementioned limitations of multimaterial 3D printing, laser sintering, and laser cutting could be solved using more suitable material and more precise machining. We selected the design dimensions of these prototypes by considering the constraints imposed by manufacturing machines, such as printing, cutting area, or process resolution. In this study, as robustness and stiffness modulation are essential criteria, we fabricate our device using the origami manufacturing technique detailed in the next section. The resulting device design is large enough to enable an easy manual assembly and folding process and have its end-effector manipulated by hand.

3.3. Origami Fabrication of the F-VSA System

The origami pattern presented in this article is novel and has been created to achieve our platform design. We wanted to create a metamaterial that would be highly reconfigurable to play with the inherent stiffness of its joints. We were strongly inspired by the kirigami pattern and folding process presented by Neville,[51] but changed the honeycombs into squares, constraining the structure to have a positive Poisson ratio. Our new pattern, as well as the folding sequence to achieve the F-VSA system, is shown in **Figure 5**. This pattern also includes holes that are visible in Figure 1. They are used to insert pins that align flexible and rigid layers during the assembly process. After creating and gluing this stack of functional layers, we fold half of the squares on themselves and insert extra water-bomb origami in the resulting interstices. The central square is the gap in which the platform, which is also an origami water-bomb, is fixed onto. This folding sequence allows the making of the internal diamonds that compress or expand to modulate the stiffness of the platform. Finally, we cut out the extra links and joints and fix the F-VSA system's external diamonds to the servo motors.

Our current prototype is made from three material layers: a 0.2 mm-thick Fr4 that is rigid and defines the system's links, a 0.05 mm-thick Kapton that creates the elastic joints, and one layer of Polymelt 701 used to glue Kapton and Fr4. First, we combine Kapton and Polymelt and laser cut the result into the patterns presented by the first step of Figure 5. With the help of alignments pins, we stack the Fr4 on the part that needs to be made rigid and fix it by melting the Polymelt using a heat press. Finally, the additional water bomb and platform are created with the same method and integrated into the main structure during the folding process by heat pressing.

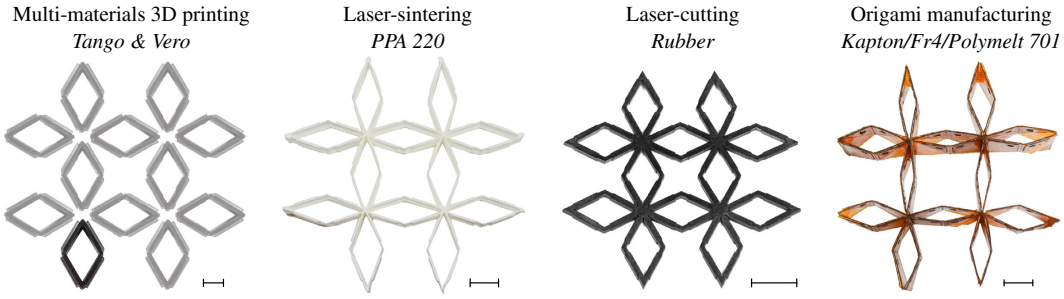

Figure 4. Proof of concept using four manufacturing methods. We explored four manufacturing strategies to fabricate our system: multimaterial 3D printing, laser sintering, laser cutting of flexible material, and origami manufacturing. All the scales of this figure have a 10 mm length. For each method, we made a proof of concept demonstrating that our design is independent of the fabrication method. Regarding the multimaterial 3D-printed prototype, only one diamond was built. We make the final prototype using the origami manufacturing method due to its robustness and ability to tune the stiffnesses of the hinges.

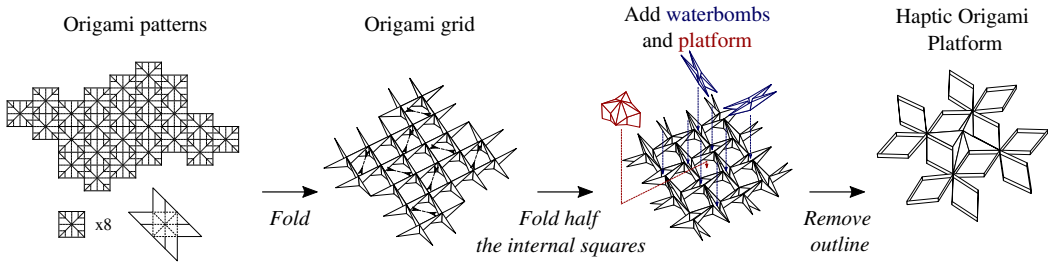

Figure 5. Origami folding sequence of the F-VSA system. First, the F-VSA system's pattern is laser cut on a flexible layer. The first folding process creates origami squares, of which half are folded on themselves to create interstices. Extra waterbombs are placed in these interstices, and the platform, also made out of a water-bomb pattern, is attached to the origami's central square. Extra external links and joints are removed from the resulting structure to create the final origami and attach it to the servo motors.

3.4. System Description for the MSA

To apply the MSA method to the F-VSA system, first, we assign the elements and nodes as described in the first step of the procedure presented in Section 2.2. The F-VSA system has 52 flexible links, 76 passive or elastic joints, and one flexible platform for a total of 109 nodes, as shown in **Figure 6**.

The links are composed of Kapton, FR4, and Polymelt. As the thickness and stiffness of Fr4 is significantly larger than the others, we assume that only the latter contribute to the link stiffness. We approximate the links as beams of 12.5 mm length, 25 mm width, and 1 mm thickness and assume FR4 Young's modulus and Poisson coefficient as 24×10^9 and 0.136.

When it comes to the joints, as shown by Figure 6, the F-VSA system model requires three types of rotary joints: one-DoF Elastic (solid ellipse), one-DoF passive (dashed ellipse), and joints with one-DoF elastic and one-DoF passive (solid and dashed ellipse). We assume that joints that are not connected to the platform are elastic joints with one rotational DoF along the $\hat{z}$ axis. The stiffnesses of joints are not identical as they are composed of a different number of layers due to our manufacturing process discussed in Appendix 7.3. Overall, the joints have four different stiffness values, as shown in Figure 6 with a color map. It is worth noting that we assume that joints shown with white color have zero stiffness because their stiffness is significantly lower than the rest. The joints connected to the central nodes $C_{1,2,3,4}$ have an elastic DoF along the $\hat{z}$ axis and a passive DoF along the $\hat{y}$ axis represented by the arrows in Figure 6a. This passive DoF is the same for the joints directly connected to the platform.

Finally, after assigning all the elements to the F-VSA system's links and joints, we apply the MSA technique[43] step by step as summarized in Section 2.2. The details of the elements' matrix are given in Appendix 7.2. Consequently, we aggregate the MSA model components in the form of (2). Then, we derive the relation between end-effector displacement $\mathbf{\Delta t}_e$ and wrench $\mathbf{W}_e$ as follows.

$$\mathbf{W}_{e(6\times1)} = (\mathbf{D}_{(6\times6)} - \mathbf{C}_{(6\times1296)} \cdot \mathbf{A}^{-1}_{(1296\times1296)} \cdot \mathbf{B}_{(1296\times6)}) \cdot \mathbf{\Delta t}_{e(6\times1)} + \mathbf{C}_{(6\times1296)} \cdot \mathbf{A}^{-1}_{(1296\times1296)} \cdot \mathbf{b}_{(1296\times1)} \tag{6}$$

from which one can extract the desired stiffness matrix

$$\mathbf{Kc}_{(6\times6)} = \mathbf{D}_{(6\times6)} - \mathbf{C}_{(6\times1296)} \cdot \mathbf{A}^{-1}_{(1296\times1296)} \cdot \mathbf{B}_{(1296\times6)} \tag{7}$$

and the force and torque values at initial condition

$$\mathbf{W}^0_{e(6\times1)} = \mathbf{C}_{(6\times1296)} \cdot \mathbf{A}^{-1}_{(1296\times1296)} \cdot \mathbf{b}_{(1296\times1)} \tag{8}$$

Using Equation (6)–(8), we can calculate the stiffness of the F-VSA's end-effector position based on its configurations. Furthermore, we can find the force output at both initial and current configurations. Thus, the proposed model allows to control the stiffness and force output of the F-VSAs.

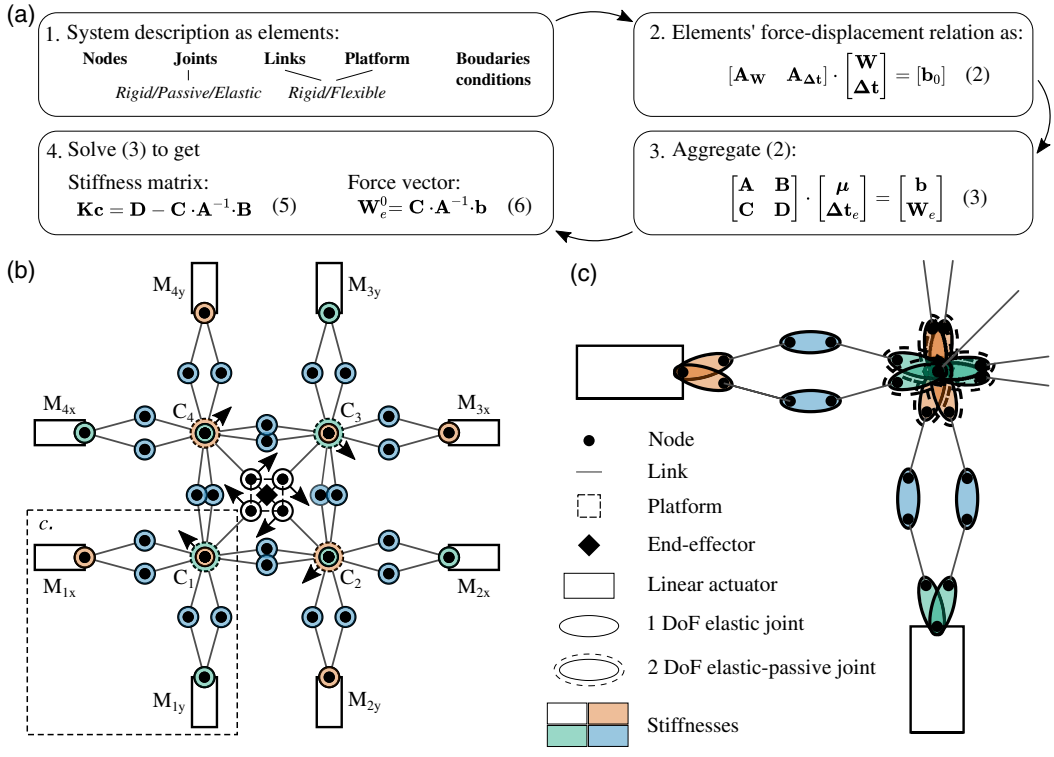

Figure 6. Description of the F-VSA system for the MSA method: a) A summary of the four steps of the MSA method. First, the system is described as five categories of elements and their associated types. For each element, write the force–displacement relation as matrix and aggregate them. Finally, in step 4, the submatrices of this aggregation allow finding the stiffness matrix and force vector relation. b,c) The locations of nodes, rigid links, and elastic and passive joints. The different stiffnesses of the joints that occur because of the folding process are indicated with a color code. b) The top view of the system and the orientation of the joints basis. The points *C* and *M* represent the four central nodes and the eight motors of the F-VSA system, respectively. c) Subpart of the F-VSA system and the nodes' locations and the stiffnesses distribution among the joints.

3.5. Force and Stiffness Control Strategy

We present a strategy to control the force and stiffness of the F-VSA system. By virtue of its interconnected compliant elements, the F-VSA system acts as a multiaxis and variable stiffness SEA. Thus, by driving the F-VSA system to a specific configuration, we actively control its stiffness and force output in $\hat{\boldsymbol{x}}$, $\hat{\boldsymbol{y}}$, $\hat{\boldsymbol{z}}$, and $\hat{\boldsymbol{\theta}}$ directions, where θ corresponds to rotation in the $\hat{\boldsymbol{z}}$ axis. To achieve that, we use eight linear actuators to modulate the position of the diamonds' attachment points. By changing the compression of the diamonds, we drive the end-effector to its new position, which minimizes the overall energy stored in all joints' virtual springs. After the configuration change, there are two cases: either the end-effector's position stays the same or is moved. In the first case, we modify the energy required to move it or, in other words, the stiffness. In the second case, we induce motion or force output at the end-effector.

To be able to change the stiffness and force output of the F-VSA system's end-effector in a controlled manner, we use the model proposed in Section 3.4. We write the Equation (6) in simplified form as follows

$$\mathbf{W}_{(6\times1)} = \mathbf{Kc}_{(6\times6)}\boldsymbol{\Delta}\mathbf{t}_{e(6\times1)} + \mathbf{W}^{0}_{e(6\times1)} \tag{9}$$

where $\mathbf{W}_{(6\times1)}$ and $\mathbf{W}^{0}_{e(6\times1)}$ are the force and torque vector felt by the user at the end-effector when its position is changed by $\boldsymbol{\Delta}\mathbf{t}_{e(6\times1)}$ displacement vector and at the initial configuration. $\mathbf{Kc}_{(6\times6)}$ is the stiffness matrix of the end-effector.

In fact, the stiffness matrix $\mathbf{Kc}_{(6\times6)}$ and wrench matrix at the initial conditions $\mathbf{W}^{0}_{e(6\times1)}$ are functions of the end-effector position and orientation and eight linear motor position inputs which are presented by $\mathbf{X}_{(6\times1)}$ and $\mathbf{U}_{(8\times1)}$ respectively. Thus, we can rewrite the Equation (9) as follows

$$\begin{aligned}\mathbf{W}_{(6\times1)} = {} & \mathbf{Kc}_{(6\times6)}(\mathbf{X}_{(6\times1)}, \mathbf{U}_{(8\times1)})\boldsymbol{\Delta}\mathbf{t}_{e(6\times1)} \\ & + \mathbf{W}^{0}_{e(6\times1)}(\mathbf{X}_{(6\times1)}, \mathbf{U}_{(8\times1)})\end{aligned} \tag{10}$$

The Equation (7) and (10) allow us to predict and control the stiffness and force output at the end-effector for a given end-effector position and orientation $\mathbf{X}_{(6\times1)}$, motor positions $\mathbf{U}_{(8\times1)}$, and end-effector displacement $\boldsymbol{\Delta}\mathbf{t}_{e(6\times1)}$. Creating and solving these equations which include the inversion of a (1296×1296) matrix take 1.5 s utilizing Julia programming language's default functions. As it is not fast enough for real-time control applications, we created a lookup table with stiffness $\mathbf{Kc}_{(6\times6)}$ and initial wrench matrix $\mathbf{W}^{0}_{e(6\times1)}$ for different end-effector $\mathbf{X}_{(6\times1)}$ and motor positions $\mathbf{U}_{(8\times1)}$.

4. Design of Experiment

In this section, we design an experimental protocol to test the F-VSA system and compare the results with the model from Section 3.4. However, the F-VSA system has many independent parameters that make the development of control algorithms challenging. For this reason, these experiments only target a reduced workspace where the lookup table of part 3.5 as control algorithm gives a direct relation between stiffness and position. First, we characterize the stiffness K of the F-VSA system at different control input values (U). Then, we implement force control at zero displacement, that is, $\boldsymbol{x} = 0$.

4.1. Experimental Setup

As shown in **Figure 7**a, we designed an experimental setup, to measure the end-effector force in the entire range of motion of the F-VSA system. This setup consists of three linear motors (Fuyu motion) for enforcing displacement on the F-VSA system end-effector in the x, y, and z directions and a servo motor for enforcing rotational displacement in the $\hat{\boldsymbol{\theta}}$ axis. The x and y linear motors are stacked on each other, and the medium-density fiberboard (MDF) frame of the F-VSA system is rigidly fixed to the $\hat{\boldsymbol{y}}$-axis linear motor, as shown in Figure 7. Similarly, the rotational servo motor is affixed on the $\hat{\boldsymbol{z}}$-axis linear motor and rigidly connected to the end-effector of the F-VSA system. Attaching the F-VSA system to the experimental setup is challenging because of the complex motion of its end-effector. To address this, we designed a custom 3D-printed attachment that fixes the end-effector to the force sensor. This attachment consists of four 4-bar linkages attached to the four vertices of the out-of-plane mechanism. During characterization, the four-bar linkages convert the upward motion of the $\hat{\boldsymbol{z}}$-axis linear motor into horizontal motion, which compresses the water-bomb diagonally and generates the out-of-plane motion. When moved in the x, y, or θ directions, this attachment also rigidly holds the water-bomb position at the desired displacement. A Nano17 six-axis force sensor ATI Industrial Automation, force resolution, 12.5 mN, is affixed to the servo motor and measures the interaction forces. Finally, to control and communicate with the F-VSA system, we use an Arduino Mega and a custom robot operating system (ROS) package consisting of control algorithms and graphical user interface (GUI).

4.2. Stiffness Modulation Experiment

We characterize the passive structural stiffness of the F-VSA system for different sets of control inputs to the servo motors. In this study, we only consider homogeneous inputs wherein all the motors have the same displacement from their resting position: 0, 1, 2, 3, 4, or 5 mm. Here, a motor displacement of 0 mm corresponds to its resting position when all the diamonds are fully extended and the end-effector cannot move. At a motor displacement of 5 mm, the end-effector can move a much larger distance. Thus, we see that the motion range of the end-effector depends on the motor displacement due to the flattening of the diamond patterns when fully extended. Similarly, they are also prone to collision with neighboring diamond patterns. To address this, we developed a custom algorithm presented in Appendix 7.1 that calculates the allowable range of motion of the end-effector along the 4-DoF for the given control input value.

For every motor input condition, [0, 1, 2, 3, 4, 5 mm], we first find the range of motion of the end-effector in $\hat{\boldsymbol{x}}$, $\hat{\boldsymbol{y}}$, $\hat{\boldsymbol{z}}$, and $\hat{\boldsymbol{\theta}}$ using the aforementioned algorithm. We then define a grid of all possible points in the $\boldsymbol{xyz\theta}$ space, with a resolution of 1 mm

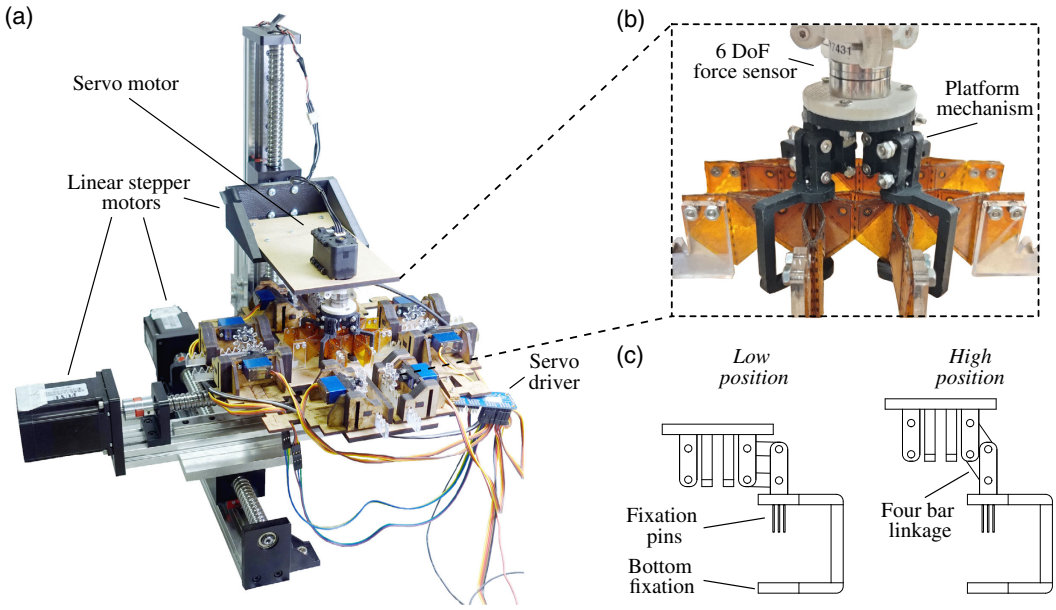

Figure 7. Experimental setup design to measure the end-effector force of the F-VSA system in all the workspace. a) The platform that uses three linear stages to move the end-effector along the $\hat{x}$, $\hat{y}$, and $\hat{z}$ axis. In addition, we use a servo motor to rotate the end-effector with an angle $\hat{\theta}$. b) In this experimental setup, we replace the origami platform with a custom 3D-printed one with the same mechanical behavior. The latter allows to connect the 6-DoF force sensor between the servo motor and F-VSA system. c) Fixation pins allow to correctly position and tighten the connection between platform and F-VSA system. In addition, to avoid unwanted motion of the attach between these two elements, we constrain the F-VSA system laterally with a four-bar linkage mechanism and vertically using a bottom stopper.

in $\hat{x}$, $\hat{y}$, and $\hat{z}$ axes, and 5 in the $\hat{\theta}$ axis. We then move the end-effector to each of these points sequentially using the experimental setup, measure the output force for two seconds, and record the average value.

4.3. Force Control Experiment

Using the model described in Section 3.4, we demonstrate force control with the F-VSA system. We define a force field in the x-y space using the F-VSA system to deliver the desired output. This virtual field of forces $\vec{f}$ is defined in the form of a vortex, as shown in Figure 9b, and is characterized by the following linear mapping.

$$\|\vec{f}\| = \begin{cases} 0 & \text{if dist} = 0 \\ f_{max}\frac{\text{dist}_{max}-\text{dist}}{\text{dist}_{max}} & \text{else} \end{cases} \tag{11}$$

$$\text{Angle}(\vec{f}) = \text{Angle}(\vec{cp}) - \frac{\pi}{2} - \alpha \tag{12}$$

where dist is the distance between the vortex center C and the virtual point P position. The maximal distance that can be reached by P is $\text{dist}_{\max}$. The maximal force amplitude $f_{\max}$ is reached for $\text{dist} = 0$. Finally, α is an angle offset that orients the vectors toward the center.

Using the experimental setup, we validate if the F-VSA system can generate the above force field. To do so, we define a grid of 100 points in the virtual x-y space of the system, as shown in Figure 9b. For each point, we do the following steps: 1) Calculate the desired force output using Equation (11) and (12).

Table 1. Relation between force vector set point and pair motors to activate as control input.

	Force X	Force Y
(+)	$M_{1x} - M_{4x}$	$M_{1y} - M_{2y}$
(−)	$M_{2x} - M_{3x}$	$M_{3y} - M_{4y}$

2) Calculate the F-VSA system motor inputs that can provide this force using the lookup table defined in Section 3.5. As this experiment only considers 2D force control, we simplify the control problem using only pairs of motors to generate forces along the $\hat{x}$ and $\hat{y}$ directions. The link between forces direction and corresponding motor pair is given by **Table 1**. 3) Move the eight motors to the calculated positions to render the desired interaction force. 4) Measure the force applied by the F-VSA system in $\hat{x}$ and $\hat{y}$ axes using the experimental setup. 5) Move the virtual cursor to the next point.

Starting from index point 0, we carry out the steps above and traverse through each point of the grid from index 0 to 99.

5. Experimental Results

This section presents and analyzes the results of the experiments described in Section 4. First, we assess the precision of our model by comparing the predicted value with the measure of the force at the end-effector. Then, the second experiment demonstrates that controlling the end-effector force at zero displacement is achievable.

5.1. Stiffness Modulation Results

The result of the experiment presented by 4.2 is represented by **Figure 8** that shows four graphs associated with the 4-DoF of the end-effector motion: x, y, z, and θ. For ease of presentation, we only show the results corresponding to the end-effector displacement in a single axis at a time. The top-left and -right graphs correspond to the force output during uniaxial displacement in $\hat{x}$ and $\hat{y}$ axes, respectively. Similarly, the bottom-left and -right graphs correspond to uniaxial displacement in $\hat{z}$ and $\hat{\theta}$ axes, respectively. In all graphs, the markers correspond to the measured data, and the continuous curves correspond to the model prediction. The different colors correspond to the control inputs. From Figure 8, we see that for different motor inputs, the passive stiffness at the end-effector is different with the largest change in the $\hat{x}$, $\hat{y}$, and $\hat{z}$ axes.

For the $\hat{x}$ and $\hat{y}$ axes, the end-effector force acts diagonally across the diamond patterns and therefore induces a moment at the compliant hinges. With increasing motor input, the moment arm of this diagonal force increases, inducing a larger moment. As a result, we see a decrease in the end-effector stiffness with an increase in motor input. In the $\hat{z}$ axis, the external diamonds extend for a positive displacement and compress for a negative displacement. Similarly, the forces are also transformed into diagonal forces during displacement in the $\hat{z}$ axis. Therefore, we observe a similar pattern for the $\hat{z}$ axis' stiffness that decreases with increasing motor displacement. Finally, during rotation along the $\hat{\theta}$ axis, four of the external diamonds are extended, and four are compressed. These two effects cancel each other up to some extent, which is why we observe a lesser effect on the stiffness.

The differences between the model and measured values can be attributed to the pretension in the compliant hinges, which is due to inconsistencies in the manufacturing process. This pretension has slight dissimilarities among the different compliant joints and is difficult to assess accurately. In this experiment, we assume the joints to be identical and the resting position of the F-VSA system to be at the center. The inaccuracies of this assumption lead to the asymmetry observed between $\hat{x}$ axis and $\hat{y}$ axis results.

We reported the maximal forces generated by the F-VSA system along the $\hat{x}$, $\hat{y}$, $\hat{z}$, and $\hat{\theta}$ axis in **Table 2**.

5.2. Force Control Results

The result of the experiment described by 4.3 is given in **Figure 9**b that shows the desired versus measured forces in the force field in the area defined in the x-y space. Similarly, Figure 9c shows the desired versus measured

Table 2. The performance of the F-VSA system: the first column represents the maximal theoretical displacement, while the maximal measured forces are in the second column.

	Maximal features	
	Range of motion	Measured force
Planar translation	±12.5 mm	4.7 N
Normal translation	±8 mm	10 N
Rotation	±65°	0.41 Nm

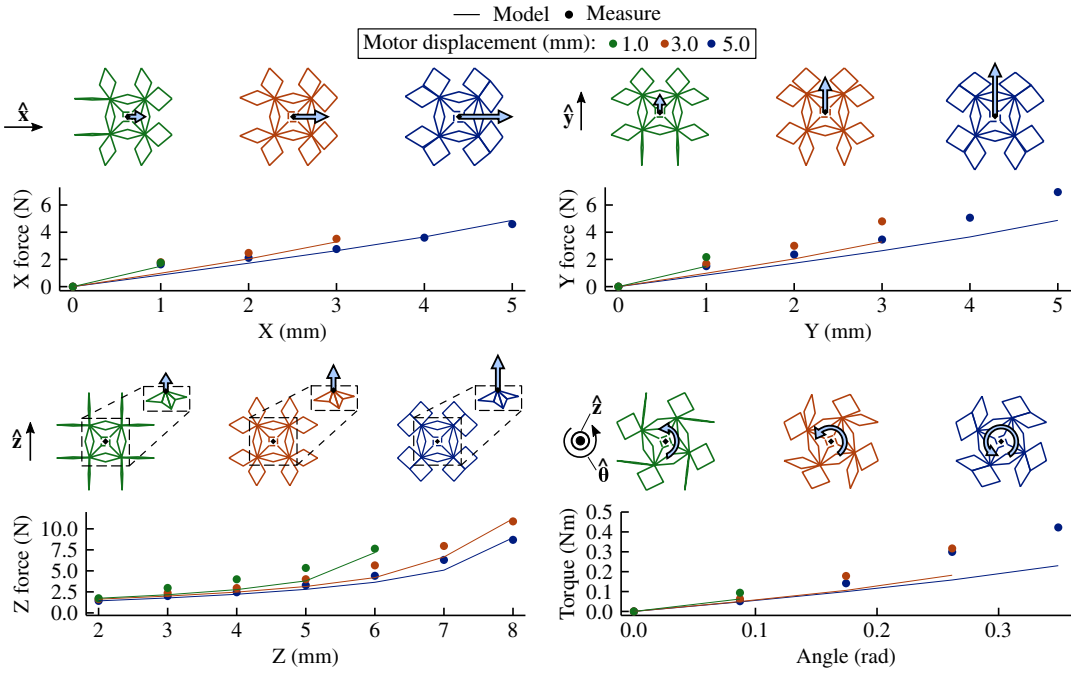

Figure 8. Stiffness characterization of the F-VSA system: comparison between the force measured (scatter plot) and predicted by our model (solid line) for the translation along two axes, rotation, and normal displacement of the F-VSA system end-effector. To reduce the problem dimensions, we only represented displacement starting from the origin and along one axis at the time for a height of 4 mm. Moreover, the motor displacement programmed for the experiment is the same for the eight servo and consists of a uniform reduction of the arms of 5 mm. The theoretical values are read from the model presented in Section 3.4.

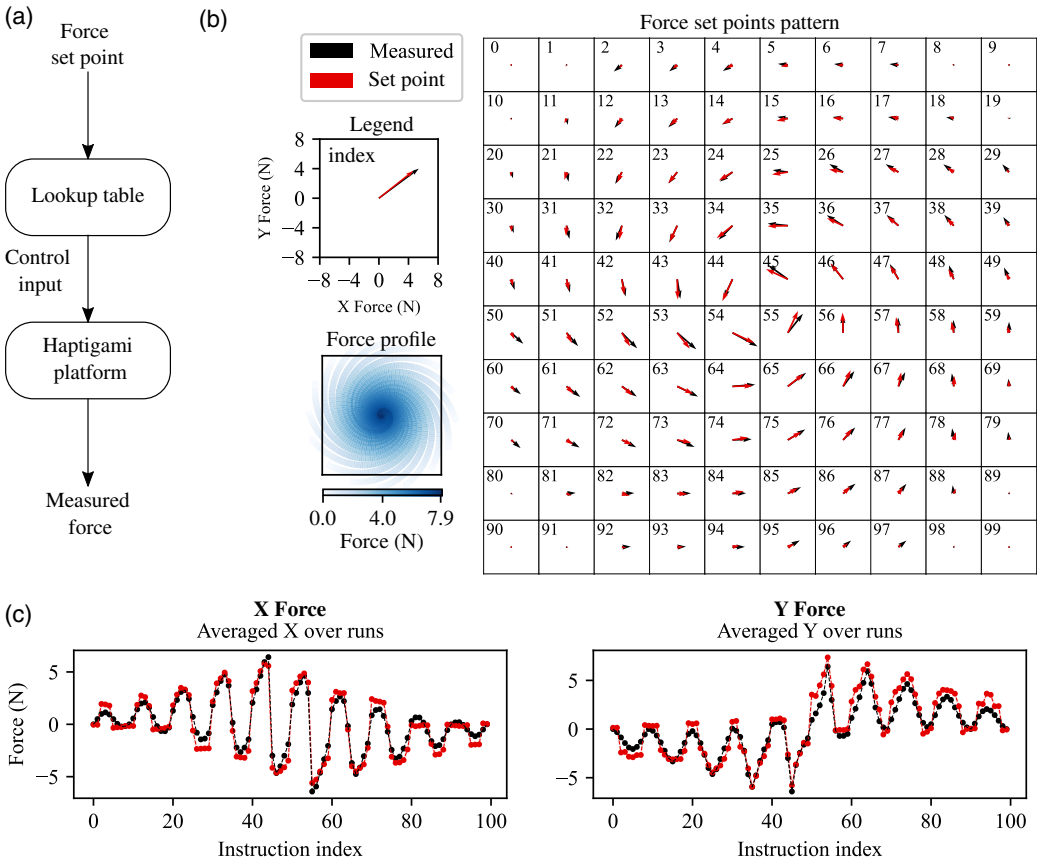

Figure 9. Control of the F-VSA system to render a vortex-shaped force field. a) Algorithm used for force tracking: a lookup table returns the motor control inputs associated with the current end-effector position input and desired force set point. In this experiment, the end-effector position is fixed and set to 0. After control of the linear actuators, we measured the force at the end-effector. b,c) The comparison between set point and the average of the measures for over four runs. We sent 100 set points in a vortex shape represented by (b) and compared it with the measured X and Y force values. The result is shown in (b) as vectors and in (c) as plots.

force values in the $\hat{x}$ and $\hat{y}$ directions, measured in sequence, while traversing through the grid points in the force field. We observe good agreement between the model and experiments with root mean square (RMS) errors of 0.74 N in $\hat{x}$ and 0.94 N in $\hat{y}$. This demonstrates the capabilities of the F-VSA system to recreate any other force field or impedance by adapting the presented method.

6. Conclusion and Future Work

SEAs and VSAs are two methods commonly used for applications requiring stable force control performance. SEAs suffer from limited bandwidth due to the constant stiffness of their elastic elements. Although VSAs offer a solution by adding the capability to vary the stiffness of elastic elements, they suffer from mechanical complexity and bulkiness as they require several components for actuation, series elasticity, transmission, and structural support. In this article, we present F-VSA, a novel method to address the mechanical complexity of VSAs. F-VSA combines the elements of elasticity, transmission, and variable stiffness using a repeated folding network made of flexure joints. These joints both define the kinematics of a system and act as virtual springs. F-VSA can render different stiffness values by modulating its geometry by virtue of its design. Thus, it significantly reduces the number of components and parts needed compared with VSAs. Furthermore, the MSA-based stiffness modeling strategy enables active control of the force and stiffness output.

Using the F-VSA method, we designed and developed a 4-DoF system with three translations and one rotation. The device can actively induce force output and motion during interaction and change its stiffness along its DoFs. To apply force and stiffness control, we modeled the device using the MSA method and characterized it to validate the model. Then, we conducted a comprehensive force control experiment and illustrated that the device successfully generates a force with any direction and amplitude within the device's boundaries. The results show that this design principle can be extended for creating a myriad of multi-DoF devices with tunable stiffness and force output.

Future studies will investigate the inverse kinematic and stiffness model. This will enable the optimization of the F-VSA system design parameters to get the desired mechanical performance in force, stiffness, and motion range adapted for a specific application. In addition, there is a need to improve the current control strategy that limits the use of the F-VSA system to configurations associated with a unique stiffness output. Second, we

will implement additional sensors to monitor metrics such as system geometry or output variables like the force or torque. This will allow closed-loop control and further improve precision. Then, future studies need to consider the plastic deformations of the F-VSA joints under large deformations,[52] which is ignored in our current MSA modeling. Finally, one assumption of this study was that the initial resting positions of the compliant joints are well known. However, inaccurate values or dissimilar resting positions among the repeating elements lead to discrepancies between the model and observed mechanical properties.

Regardless of these limitations, the work presented in this article constitutes a new approach to designing compact, scalable, variable stiffness devices with multi-DoF. Similar to VSA, this technology provides safe human–robot interactions for applications such as rehabilitation, or assistive devices. Moreover, increasing the compliant mechanisms' compactness enables the implementation of more functionalities in devices with space constraints such as wearable technologies. The F-VSA low size and numerous DoF also offer better compatibility with the human complex biomechanics and allow the development of haptic devices with numerous functionalities or enhanced control interfaces.

7. Appendix

7.1. Workplace Determination

The complex structure of the F-VSA system makes some configurations not achievable for the two following reasons. First, the diamonds cannot be extended more than two times the size of their side length. Second, during compression, the diamonds expand laterally, leading to constraints in terms of space. Indeed, the more the diamonds are compressed, the more the diamonds are prone to get in contact with each other. In this regard, we developed an algorithm able to assess if the Haptigami configuration is correct, given its motor and end-effector position. From these two inputs, this function, called *isHaptigamiCorrect*, deduces the position of all Haptigami's vertices and checks if the two aforementioned conditions are respected. To compute our device workspace, we use *isHaptigamiCorrect* inside **Algorithm 1**. The latter tests the configuration for several motor and end-effector positions and returns the list of possible configurations. The final workspace is given by Table 2 and allows 12.5 mm in x and y displacement, 65° in rotation, and 8 mm for the normal displacement.

Algorithm 1. Algorithm used to compute the possible workspace of the Haptigami.

```
motor_Pos → list of motor positions
EF_Pos → list endeffector positions in x, y, z, α
configList → empty list
for all mP in motor_Pos
  for all pos in EF_Pos
    if isHaptigamiCorrect(mP, pos)
      configList.append([mP, pos])
    end if
  end for
end for
```

7.2. Matrix Structural Analysis

As described by Section 2.2, the first step when applying the MSA method is to describe the system as a set of matrix equations. Let $\mathbf{W}_i$ and $\mathrm{D}\mathbf{t}_i$ be, respectively, the six force and six displacements variables associated with node i. As our system is composed of 109 nodes, the total number of variables is 1308. As indicated by Klimchik et al.,[43] the equations for the elements of the F-VSA system presented in Section 3.4, that is 1) flexible links, 2) flexible platform, 3) passive joints, 4) elastic joints, 5) passive/elastic joints, 6) elastic supports, and 7) external loadings, are as follows:

Flexible Links: connects two nodes i and j thought stiffness coefficients associated with the forces and stiffness variables $\mathbf{W}_i$ and $\mathbf{\Delta t}_i$. Each link gives a system of 12 equations, resulting in an aggregated matrix of 624 rows, as presented later.

$$[\{-\mathbf{I}_{ij}\} \quad \{\mathbf{K}^{ij}\}] \cdot \begin{bmatrix}\{\mathbf{W}_{ij}\}\\ \{\mathbf{\Delta t}_{ij}\}\end{bmatrix} = \mathbf{0} \tag{A1}$$

Flexible platform: is a set of n nodes connected to the end-effector thought stiffness coefficients, similar to the flexible link case. The F-VSA system has four nodes linked to the end-effector to create the platform, which results in 30 equations presented as

$$\begin{bmatrix}\{-\mathbf{I}_{ij}\} & \{\mathbf{K}^{ij}_{12x12}\}\\ \mathbf{0} & \{\mathbf{K}^{ij}_{12x12}\}\end{bmatrix} \cdot \begin{bmatrix}\{\mathbf{W}_{ij}\}\\ \{\mathbf{\Delta t}_{ij}\}\end{bmatrix} = \begin{bmatrix}\mathbf{0}\\ \mathbf{W}_{ext}\end{bmatrix} \tag{A2}$$

with *Wext* being the external force applied to the end-effector.

Passive Joints: are used to connect the F-VSA system's platform to the rest of the system. Each passive joint creates 12 equations, giving a total of 48 rows in its matrix form.

$$\begin{bmatrix}\mathbf{0} & \{\mathbf{\Lambda}^r_i, -\mathbf{\Lambda}^r_j\}\\ \{\mathbf{\Lambda}^r_i, \mathbf{\Lambda}^r_j\} & \mathbf{0}\\ \{\mathbf{\Lambda}^p_i\} & \mathbf{0}\\ \{\mathbf{\Lambda}^p_j\} & \mathbf{0}\end{bmatrix} \cdot \begin{bmatrix}\{\mathbf{W}_{ij}\}\\ \{\mathbf{\Delta t}_{ij}\}\end{bmatrix} = \mathbf{0} \tag{A3}$$

assuming all initial conditions null. In this equation, Λ is a matrix made from the joint's orthonormal basis. $\mathbf{\Lambda}^r$ is an aggregation of the base's vector along the rigid directions, while $\mathbf{\Lambda}^p$ only considers the base's vectors along which the motion is free to occur.

Elastic Joints: connect four nodes to create two joints in the F-VSA system's diamonds. Each joint creates 12 equations, giving an aggregated matrix of 288 rows. The elastic joint matrix is

$$\begin{bmatrix}\mathbf{0} & \{\mathbf{\Lambda}^r_i, -\mathbf{\Lambda}^r_j\}\\ \{\mathbf{I}_i, \mathbf{I}_j\} & \mathbf{0}\\ \{\mathbf{\Lambda}^e_i\} & \{-\mathbf{K}^e_i \mathrm{L}^e_i, \mathbf{K}^e_j \mathbf{\Lambda}^e_j\}\end{bmatrix} \cdot \begin{bmatrix}\{\mathbf{W}_{ij}\}\\ \{\mathbf{\Delta t}_{ij}\}\end{bmatrix} = \mathbf{0} \tag{A4}$$

considering the initial condition null. In this case, $\mathbf{K}^e$ is the stiffness matrix of the joint along its DoF, and $\mathbf{\Lambda}^p$ is replaced by $\mathbf{\Lambda}^e$ but serves the same function.

Passive–Elastic Joints: the planar part of the F-VSA system is connected to the popup mechanism through four passive–elastic joints. The latter are two-DoF joints whose $\hat{\boldsymbol{x}}$ axis has been rotated to point toward the platform, acting as elastic joint along the $\hat{\boldsymbol{z}}$

axis and passive joint along the $\hat{\mathbf{y}}$ axis. As all four joints are interconnected for each of the four central nodes, all four joints are interconnected, and each cluster creates 54 equations, for a total of 216 equations. The matrix of a passive–elastic joint is given by

$$\begin{bmatrix} \mathbf{0} & \{\mathbf{\Lambda}_i^r, -\mathbf{\Lambda}_j^r\} \\ \{\mathbf{\Lambda}_i^r, \mathbf{\Lambda}_j^r\} & \mathbf{0} \\ \{\mathbf{\Lambda}_i^p\} & \mathbf{0} \\ \{\mathbf{\Lambda}_i^e\} & \{-\mathbf{K}_i^e\mathbf{\Lambda}_i^e, \mathbf{K}_j^e\mathbf{\Lambda}_j^e\} \end{bmatrix} \cdot \begin{bmatrix} \{\mathbf{W}_{ij}\} \\ \{\mathbf{\Delta t}_{ij}\} \end{bmatrix} = \mathbf{0} \tag{A5}$$

with no preloading of the joints.

Elastic Support: similar to the elastic joints, they are used to connect the F-VSA system to the support. Each of them gives 6 equations, for a total of 96 equations. The matrix form of a elastic support is

$$\begin{bmatrix} \mathbf{0} & \{\mathbf{\Lambda}_i^r, -\mathbf{\Lambda}_j^r\} \\ \{\mathbf{\Lambda}_i^e\} & \{-\mathbf{K}_i^e\mathbf{\Lambda}_i^e, \mathbf{K}_j^e\mathbf{\Lambda}_j^e\} \end{bmatrix} \cdot \begin{bmatrix} \{\mathbf{W}_{ij}\} \\ \{\mathbf{\Delta t}_{ij}\} \end{bmatrix} = \mathbf{0} \tag{A6}$$

with no preloading of the joints.

External Loadings: apply the following set of equations for every node is applied under an external wrench $\mathbf{W_e}$

$$[-\mathbf{I}_{6\times6} \quad \mathbf{0}] \cdot \begin{bmatrix} \{\mathbf{W}_{ij}\} \\ \{\mathbf{\Delta t}_{ij}\} \end{bmatrix} = \mathbf{W_e} \tag{A7}$$

Concatenating Equation (A1) to (A7) while making sure to aggregate the platform equation finally gives the system of Equation (2). Finally, **A**, **B**, **C**, and **D** can be extracted from this matrix and we use Equation (4).

7.3. Modeling Example: MSA Applied to a Diamond

This subsection applied the method described in Section 2.2 to a single diamond of the system described by nodes 1–9 in Figure 6 b. It is worth noting that the F-VSA system's stiffness can only be found using the MSA to the whole system at once. Therefore, this subsection is just a detailed example to help the reader understand how to apply the MSA to a simple submechanism (**Figure 10**).

7.3.1. System Description and Force–Displacement Relations

As represented by Figure 6b, a single diamond is composed of nine nodes that define four links and six joints. The total number of variables is

$$\text{number of nodes} \times 6 \text{ displacements vars} \times 6 \text{ wrench vars} \tag{A8}$$

hence 108.

Flexible Links: Four links give a total of 48 equations, leading to the following matrix

$$\begin{bmatrix} -\mathbf{I}_{12\times12} & \mathbf{0} & \mathbf{0} & \mathbf{0} & \mathbf{K}_{12\times12}^{12} & \mathbf{0} & \mathbf{0} & \mathbf{0} \\ \mathbf{0} & -\mathbf{I}_{12\times12} & \mathbf{0} & \mathbf{0} & \mathbf{0} & \mathbf{K}_{12\times12}^{34} & \mathbf{0} & \mathbf{0} \\ \mathbf{0} & \mathbf{0} & -\mathbf{I}_{12\times12} & \mathbf{0} & \mathbf{0} & \mathbf{0} & \mathbf{K}_{12\times12}^{56} & \mathbf{0} \\ \mathbf{0} & \mathbf{0} & \mathbf{0} & -\mathbf{I}_{12\times12} & \mathbf{0} & \mathbf{0} & \mathbf{0} & \mathbf{K}_{12\times12}^{78} \end{bmatrix}_{48\times108} \tag{A9}$$

Elastic Joints and Support: We assume all joints elastic with a stiffness k and one-DoF along $\hat{\mathbf{z}}$. Therefore, one can write

$$\mathbf{\Lambda}^r = \begin{bmatrix} 1 & 0 & 0 & 0 & 0 & 0 \\ 0 & 1 & 0 & 0 & 0 & 0 \\ 0 & 0 & 1 & 0 & 0 & 0 \\ 0 & 0 & 0 & 1 & 0 & 0 \\ 0 & 0 & 0 & 0 & 1 & 0 \end{bmatrix}; \mathbf{\Lambda}^e = [0 \quad 0 \quad 0 \quad 0 \quad 0 \quad 1] \tag{A10}$$

The joints between nodes 2,3 and 6,7 create 24 equations and lead to the following matrix

$$\begin{bmatrix} \mathbf{0} & \mathbf{0} & \mathbf{0} & \mathbf{0} & \mathbf{0} & \mathbf{0} & \mathbf{0} & \mathbf{0} & \mathbf{0} & \mathbf{0} & \mathbf{\Lambda}^r & -\mathbf{\Lambda}^r & \mathbf{0} & \mathbf{0} & \mathbf{0} & \mathbf{0} & \mathbf{0} & \mathbf{0} \\ \mathbf{0} & \mathbf{0} & \mathbf{0} & \mathbf{0} & \mathbf{0} & \mathbf{0} & \mathbf{0} & \mathbf{0} & \mathbf{0} & \mathbf{0} & \mathbf{0} & \mathbf{0} & \mathbf{0} & \mathbf{0} & \mathbf{\Lambda}^r & -\mathbf{\Lambda}^r & \mathbf{0} & \mathbf{0} \\ \mathbf{0} & \mathbf{I} & \mathbf{I} & \mathbf{0} & \mathbf{0} & \mathbf{0} & \mathbf{0} & \mathbf{0} & \mathbf{0} & \mathbf{0} & \mathbf{0} & \mathbf{0} & \mathbf{0} & \mathbf{0} & \mathbf{0} & \mathbf{0} & \mathbf{0} & \mathbf{0} \\ \mathbf{0} & \mathbf{0} & \mathbf{0} & \mathbf{0} & \mathbf{0} & \mathbf{I} & \mathbf{I} & \mathbf{0} & \mathbf{0} & \mathbf{0} & \mathbf{0} & \mathbf{0} & \mathbf{0} & \mathbf{0} & \mathbf{0} & \mathbf{0} & \mathbf{0} & \mathbf{0} \\ \mathbf{0} & \mathbf{\Lambda}^e & \mathbf{0} & \mathbf{0} & \mathbf{0} & \mathbf{0} & \mathbf{0} & \mathbf{0} & \mathbf{0} & \mathbf{0} & k\mathbf{\Lambda}^e & -k\mathbf{\Lambda}^e & \mathbf{0} & \mathbf{0} & \mathbf{0} & \mathbf{0} & \mathbf{0} & \mathbf{0} \\ \mathbf{0} & \mathbf{0} & \mathbf{0} & \mathbf{0} & \mathbf{0} & \mathbf{\Lambda}^e & \mathbf{0} & \mathbf{0} & \mathbf{0} & \mathbf{0} & \mathbf{0} & \mathbf{0} & \mathbf{0} & \mathbf{0} & k\mathbf{\Lambda}^e & -k\mathbf{\Lambda}^e & \mathbf{0} & \mathbf{0} \end{bmatrix}_{24\times108} \tag{A11}$$

As the joints between 4, 9, and 5 are grouped, we can combine 6 equations and write the 18 equation system such as

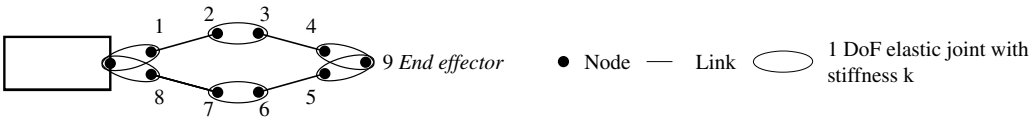

Figure 10. MSA model of a single diamond: A single diamond and its end-effector is modeled by nine nodes, four links, and six joints. We consider the links flexible and the joints elastic along one-DoF with stiffness k. The linear actuator is considered as the support and the floating node nine as the end-effector.

$$\begin{bmatrix} \mathbf{0} & \mathbf{0} & \mathbf{0} & \mathbf{0} & \mathbf{0} & \mathbf{0} & \mathbf{0} & \mathbf{0} & \mathbf{0} & \mathbf{0} & \mathbf{0} & \mathbf{0} & \mathbf{0} & \mathbf{0} & \mathbf{0} & \mathbf{0} & \mathbf{0} & -\mathbf{\Lambda}^r \\ \mathbf{0} & \mathbf{0} & \mathbf{0} & \mathbf{0} & \mathbf{0} & \mathbf{0} & \mathbf{0} & \mathbf{0} & \mathbf{0} & \mathbf{0} & \mathbf{0} & \mathbf{0} & \mathbf{0} & \mathbf{\Lambda}^r & \mathbf{0} & \mathbf{0} & \mathbf{0} & -\mathbf{\Lambda}^r \\ \mathbf{0} & \mathbf{0} & \mathbf{0} & \mathbf{I} & \mathbf{I} & \mathbf{0} & \mathbf{0} & \mathbf{0} & \mathbf{0} & \mathbf{0} & \mathbf{0} & \mathbf{0} & \mathbf{0} & \mathbf{0} & \mathbf{0} & \mathbf{0} & \mathbf{0} & \mathbf{I} \\ \mathbf{0} & \mathbf{0} & \mathbf{0} & \mathbf{\Lambda}^e & \mathbf{0} & \mathbf{0} & \mathbf{0} & \mathbf{0} & \mathbf{0} & \mathbf{0} & \mathbf{0} & \mathbf{0} & k\mathbf{\Lambda}^e & \mathbf{0} & \mathbf{0} & \mathbf{0} & \mathbf{0} & -k\mathbf{\Lambda}^e \\ \mathbf{0} & \mathbf{0} & \mathbf{0} & \mathbf{0} & \mathbf{\Lambda}^e & \mathbf{0} & \mathbf{0} & \mathbf{0} & \mathbf{0} & \mathbf{0} & \mathbf{0} & \mathbf{0} & \mathbf{0} & k\mathbf{\Lambda}^e & \mathbf{0} & \mathbf{0} & \mathbf{0} & -k\mathbf{\Lambda}^e \end{bmatrix}_{18\times 108} \tag{A12}$$

Finally, this system has two elastic joints linked to the support which lead to 12 equations

$$\begin{bmatrix} \mathbf{0} & \mathbf{0} & \mathbf{0} & \mathbf{0} & \mathbf{0} & \mathbf{0} & \mathbf{0} & \mathbf{0} & \mathbf{0} & \mathbf{\Lambda}^r & \mathbf{0} & \mathbf{0} & \mathbf{0} & \mathbf{0} & \mathbf{0} & \mathbf{0} & \mathbf{0} & \mathbf{0} \\ \mathbf{0} & \mathbf{0} & \mathbf{0} & \mathbf{0} & \mathbf{0} & \mathbf{0} & \mathbf{0} & \mathbf{0} & \mathbf{0} & \mathbf{0} & \mathbf{0} & \mathbf{0} & \mathbf{0} & \mathbf{0} & \mathbf{0} & \mathbf{0} & \mathbf{\Lambda}^r & \mathbf{0} \\ \mathbf{\Lambda}^e & \mathbf{0} & \mathbf{0} & \mathbf{0} & \mathbf{0} & \mathbf{0} & \mathbf{0} & \mathbf{0} & \mathbf{0} & -k\mathbf{\Lambda}^e & \mathbf{0} & \mathbf{0} & \mathbf{0} & \mathbf{0} & \mathbf{0} & \mathbf{0} & \mathbf{0} & \mathbf{0} \\ \mathbf{0} & \mathbf{0} & \mathbf{0} & \mathbf{0} & \mathbf{0} & \mathbf{0} & \mathbf{0} & \mathbf{\Lambda}^e & \mathbf{0} & \mathbf{0} & \mathbf{0} & \mathbf{0} & \mathbf{0} & \mathbf{0} & \mathbf{0} & \mathbf{0} & -k\mathbf{\Lambda}^e & \mathbf{0} \end{bmatrix}_{12\times 108} \tag{A13}$$

External loadings: are used to constrain the system at the end-effector. We assume that no load is applied on the end-effector, that is, $\mathbf{W_e} = \mathbf{0}$

$$[\mathbf{0}\ \mathbf{0}\ \mathbf{0}\ \mathbf{0}\ \mathbf{0}\ \mathbf{0}\ \mathbf{0}\ \mathbf{0}\ -\mathbf{I}\ \mathbf{0}\ \mathbf{0}\ \mathbf{0}\ \mathbf{0}\ \mathbf{0}\ \mathbf{0}\ \mathbf{0}\ \mathbf{0}\ \mathbf{0}]_{6\times 108} \tag{A14}$$

gives the last six equations.

7.3.2. Matrix Aggregation

Concatenating Equation (A8)–(A15) gives the following system

$$\begin{bmatrix} \mathbf{A}_{102\times 102} & \mathbf{B}_{102\times 6} \\ \mathbf{C}_{6\times 102} & \mathbf{D}_{6\times 6} \end{bmatrix} \cdot \begin{bmatrix} \boldsymbol{\mu} \\ \boldsymbol{\Delta t}_e \end{bmatrix} = \mathbf{0}_{102\times 1} \tag{A15}$$

with A an invertible square matrix.

7.3.3. Solving the System

Finally, as shown in 2.2, we use Equation (4) and (5) to find the stiffness matrix $\mathbf{Kc}_{6\times 6}$ or the constant force component $\mathbf{W_e^0}$.

Supporting Information

Supporting Information is available from the Wiley Online Library or from the author.

Acknowledgements

The authors would like to thank Professor Klimchik for his recommendations regarding the implementation of the stiffness model. His experience was helpful and allowed us to improve our understanding, model, and overall code. The authors are also grateful to M. Maxime Riou for significantly improving the manufacturing, design, and characterization setup of the F-VSA system during his master thesis. Finally, Dr. Sagar Joshi did a careful and thoughtful review of this manuscript that strongly enhanced the readability and overall content structure.

Conflict of Interest

The authors declare no conflict of interest.

Data Availability Statement

The data that support the findings of this study are available from the corresponding author upon reasonable request.

Keywords

flexure mechanisms, force controls, series elastic actuators, stiffness modulations, variable stiffness actuators

Received: December 28, 2021
Revised: March 28, 2022
Published online: June 22, 2022

[1] M. A. Robertson, H. Sadeghi, J. M. Florez, J. Paik, *Soft Robot.* **2017**, *4*, 23.
[2] Q. Xie, T. Wang, S. Yao, Z. Zhu, N. Tan, S. Zhu, *Smart Mater. Struct.* **2020**, *29*, 125017.
[3] N. Kellaris, V. Gopaluni Venkata, G. M. Smith, S. K. Mitchell, C. Keplinger, *Sci. Robot.* **2018**, *3*, eaar3276.
[4] X. Ji, X. Liu, V. Cacucciolo, Y. Civet, A. El Haitami, S. Cantin, Y. Perriard, H. Shea, *Adv. Funct. Mater.* **2021**, *31*, 2006639.
[5] W. Wang, S.-H. Ahn, *Soft Robot.* **2017**, *4*, 379.
[6] J. Walker, T. Zidek, C. Harbel, S. Yoon, F. S. Strickland, S. Kumar, M. Shin, *Actuators* **2020**, *9*, 3.
[7] P. Boyraz, G. Runge, A. Raatz, *Actuators* **2018**, *7*, 48.
[8] J. Zhou, Y. Chen, Y. Hu, Z. Wang, Y. Li, G. Gu, Y. Liu, *Soft Robot.* **2020**, *7*, 743.
[9] Y. S. Narang, J. J. Vlassak, R. D. Howe, *Adv. Funct. Mater.* **2018**, *28* 1707136.
[10] Y.-F. Zhang, N. Zhang, H. Hingorani, N. Ding, D. Wang, C. Yuan, B. Zhang, G. Gu, Q. Ge, *Adv. Funct. Mater.* **2019**, *29*, 1806698.
[11] M. Pan, C. Yuan, X. Liang, T. Dong, T. Liu, J. Zhang, J. Zou, H. Yang, C. Bowen, *Adv. Intell. Syst.* **2021**, 2100140.
[12] N. El-Atab, R. B. Mishra, F. Al-Modaf, L. Joharji, A. A. Alsharif, H. Alamoudi, M. Diaz, N. Qaiser, M. M. Hussain, *Adv. Intell. Syst.* **2020**, *2*, 2000128.
[13] G. A. Pratt, M. M. Williamson, in *Proc. 1995 IEEE/RSJ Int. Conf. on Intelligent Robots and Systems. Human Robot Interaction and Cooperative Robots*, Vol. *1*, IEEE, Piscataway, NJ **1995** pp. 399–406.
[14] H. Vallery, J. Veneman, E. Van Asseldonk, R. Ekkelenkamp, M. Buss, H. Van Der Kooij, *IEEE Robot. Automat. Mag.* **2008**, *15*, 60.
[15] C. Lee, S. Kwak, J. Kwak, S. Oh, *Actuators* **2017**, *6*, 26.
[16] P. Agarwal, J. Fox, Y. Yun, M. K. O'Malley, A. D. Deshpande, *Int. J. Robot. Res.* **2015**, *34*, 1747.

[17] A. Baldoni, M. Cempini, M. Cortese, S. Crea, M. C. Carrozza, N. Vitiello, *Mechatronics* **2018**, *49* 149.
[18] A. L. Junior, R. M. de Andrade, A. Bento Filho, *Recent Adv. Robot. Syst.* **2016**, *203*.
[19] Y.-H. Lai, S.-Y. Huang, C.-C. Lan, *IEEE Robot. Automat. Lett.* **2021**, *7*, 1340.
[20] B. Vanderborght, A. Albu-Schäffer, A. Bicchi, E. Burdet, D. G. Caldwell, R. Carloni, M. Catalano, O. Eiberger, W. Friedl, G. Ganesh, M. Garabini, M. Grebenstein, G. Grioli, S. Haddadin, H. Hoppner, A. Jafari, M. Laffranchi, D. Lefeber, F. Petit, S. Stramigioli, N. Tsagarakis, M. Van Damme, R. Van Ham, L.C. Visser, S. Wolf, *Robot. Autonom. Syst.* **2013**, *61*, 1601.
[21] A. Lelevé, T. McDaniel, C. Rossa, *Front. Virt. Reality* **2020**, *1* 3.
[22] F. Conti, O. Khatib, *Int. J. Robot. Res.* **2009**, *28*, 834.
[23] J. Hurst, A. Rizzi, D. Hobbelen, in *Int. Conf. on Climbing and Walking Robots*, **2004**.
[24] R. V. Ham, T. Sugar, B. Vanderborght, K. Hollander, D. Lefeber, *IEEE Robot. Automat. Mag.* **2009**, *3*, 81.
[25] A. Bicchi, G. Tonietti, M. Bavaro, M. Piccigallo, in *Robotics Research. The Eleventh Inter. Symp*. Springer, New York **2005**, pp. 527–536.
[26] S. Wolf, G. Grioli, O. Eiberger, W. Friedl, M. Grebenstein, H. Höppner, E. Burdet, D. G. Caldwell, R. Carloni, M. G. Catalano, D. Lefeber, S. Stramigioli, N. Tsagarakis, M. Van Damme, R. Van Ham, B. Vanderborght, L. C. Visser, A. Bicchi, A. Albu-Schaffer, *IEEE/ASME Trans. Mechatron.* **2015**, *21*, 2418.
[27] X. Li, H. Zhu, W. Lin, W. Chen, K. H. Low, *IEEE Trans. Industr. Electron.* **2020**, *68*, 12452.
[28] J. Luo, S. Wang, Y. Zhao, Y. Fu, *Intell. Serv. Robot.* **2018**, *11*, 225.
[29] S. H. Lee, H. J. Lee, K. H. Lee, K. T. Nam, J. C. Koo, *Microsyst. Technol.* **2020**, *26* 3395.
[30] A. Jafari, H. Q. Vu, F. Iida, *J. Intell. Robot. Syst.* **2016**, *82*, 435.
[31] F. H. Giraud, S. Joshi, J. Paik, *IEEE Trans. Haptics* **2021**.
[32] M. Mete, J. Paik, *IEEE Robot. Automat. Lett.* **2021**, *6*, 8213.
[33] Z. Zhakypov, K. Mori, K. Hosoda, J. Paik, *Nature* **2019**, *571*, 381.
[34] R. Wood, S. Avadhanula, R. Sahai, E. Steltz, R. Fearing, *J. Mech. Des.* **2008**, *130*, 052304.
[35] D. Rus, C. Sung, *Sci. Robot.* **2018**, *3*, eaat0938.
[36] D. Rus, M. T. Tolley, *Nat. Rev. Mater.* **2018**, *3*, 101.
[37] G. Palli, G. Berselli, C. Melchiorri, G. Vassura, **2011**.
[38] H. Xin, G. Chen, B. Li, in *IEEE 9th Annual Int. Conf. on CYBER Technology in Automation, Control, and Intelligent Systems (CYBER)*. IEEE, Piscataway, NJ **2019**, pp. 370–374.
[39] P. Bilancia, G. Berselli, G. Palli, *Robot. Computer-Integr. Manufact.* **2020**, *65* 101886.
[40] H. C. Martin, Mcgraw-Hill Book Co, New York, **1966**. p. 331.
[41] C. Gosselin, *IEEE Trans. Robot. Automat.* **1990**, *6*, 377.
[42] K.-J. Bathe, *Wiley Encyclopedia of Computer Science and Engineering*, **2007**, pp. 1–12.
[43] A. Klimchik, A. Pashkevich, D. Chablat, *Mech. Mach. Theory* **2019**, *133* 365.
[44] A. Klimchik, A. Pashkevich, D. Chablat, *Finite Elements Anal. Des.* **2013**, *75* 19.
[45] F. H. Giraud, Z. Zhakypov, J. Paik, in *IEEE/RSJ Int. Conf. on Intelligent Robots and Systems (IROS)*, IEEE, Piscataway, NJ **2019** pp. 2700–2707.
[46] A. Firouzeh, J. Paik, *J. Mech. Robot.* **2015**, *7*, 021009.
[47] J. Paik, *Nat. Rev. Mater.* **2018**, *3*, 81.
[48] Z. Zhakypov, J. Paik, *IEEE Trans. Robot.* **2018**, *34*, 151.
[49] J.-L. Huang, Z. Zhakypov, H. Sonar, J. Paik, *Int. J. Robot. Res.* **2018**, *37*, 629.
[50] R. Malka, A. L. Desbiens, Y. Chen, R. J. Wood, in *IEEE/RSJ Int. Conf. on Intelligent Robots and Systems*. IEEE, Piscataway, NJ **2014**, pp. 2879–2885.
[51] R. M. Neville, F. Scarpa, A. Pirrera, *Sci. Rep.* **2016**, *6*, 1.
[52] B. Y. Dharmadasa, H. Mallikarachchi, F. Lopez Jimenez, in *AIAA Spacecraft Structures Conf.*, American Institute of Aeronautics and Astronautics, Kissimmee, Florida **2018** p. 0450.